**ORIGINAL ARTICLE**

# Registration of vascular structures using a hybrid mixture model

Siming Bayer[1] · Zhiwei Zhai[2] · Maddalena Strumia[3] · Xiaoguang Tong[4] · Ying Gao[5] · Marius Staring[2] ·
Berend Stoel[2] · Rebecca Fahrig[3] · Arya Nabavi[6] · Andreas Maier[1] · Nishant Ravikumar[1]

**Abstract**

**Purpose** Morphological changes to anatomy resulting from invasive surgical procedures or pathology, typically alter the surrounding vasculature. This makes it useful as a descriptor for feature-driven image registration in various clinical applications. However, registration of vasculature remains challenging, as vessels often differ in size and shape, and may even miss branches, due to surgical interventions or pathological changes. Furthermore, existing vessel registration methods are typically designed for a specific application. To address this limitation, we propose a generic vessel registration approach useful for a variety of clinical applications, involving different anatomical regions.

**Methods** A probabilistic registration framework based on a hybrid mixture model, with a refinement mechanism to identify missing branches (denoted as HdMM+) during vasculature matching, is introduced. Vascular structures are represented as 6-dimensional hybrid point sets comprising spatial positions and centerline orientations, using Student's $t$-distributions to model the former and Watson distributions for the latter.

**Results** The proposed framework is evaluated for intraoperative brain shift compensation, and monitoring changes in pulmonary vasculature resulting from chronic lung disease. Registration accuracy is validated using both synthetic and patient data. Our results demonstrate, HdMM+ is able to reduce more than 85% of the initial error for both applications, and outperforms the state-of-the-art point-based registration methods such as coherent point drift and Student's $t$-distribution mixture model, in terms of mean surface distance, modified Hausdorff distance, Dice and Jaccard scores.

**Conclusion** The proposed registration framework models complex vascular structures using a hybrid representation of vessel centerlines, and accommodates intricate variations in vascular morphology. Furthermore, it is generic and flexible in its design, enabling its use in a variety of clinical applications.

**Keywords** Non-rigid registration · Point matching · Brain shift · Pulmonary vascular diseases

## Introduction

A crucial component of noninvasive disease monitoring and interventional guidance systems is the registration of serially acquired intra-patient image data. As blood vessels permeate through all organs within the body, they are a rich descriptor for feature-driven image registration techniques. Vascular structures can be visualized with high-resolution images in real time, using state-of-the-art interventional and diagnostic imaging modalities. Hence, registration of vascular structures provides a good basis for registering preoperative and intraoperative images, necessary for image-guided procedures, and a noninvasive mechanism for monitoring disease progression.

Vascular image registration techniques can be categorized into point-, graph- and curve-based approaches [16]. The

✉ Siming Bayer
    siming.bayer@fau.de

1   Pattern Recognition Lab, Friedrich-Alexander University, Martenstraße 3, 91058 Erlangen, Germany

2   Leiden University Medical Center, Albinusdreef 2, 2333 ZA Leiden, The Netherlands

3   Siemens Healthcare GmbH, Siemensstraße 1, 91301 Forchheim, Germany

4   Tianjin Huanhu Hospital, Nankai University, Jizhao Road 6, Tianjin 300350, China

5   Siemens Healthineers Ltd, Wanjing Zhonghuan Nanlu, Beijing 100102, China

6   Department of Neurosurgery, Nordstadt Hospital, KRH, Haltenhoffstr 41, 30167 Hannover, Germany

main benefits of point-based approaches to vessel matching are, that they do not require *a priori* identification of correspondences; and may be imbued with robustness to outliers and missing data, by formulating the problem within a probabilistic framework [22]. Proposed the coherent point drift (CPD) algorithm for point set registration based on Gaussian mixture models (GMMs). Here, a uniform distribution component was used to account for noise and outliers. Consequently, prior knowledge about the degree of outliers present in the data has a great impact on the registration accuracy. Compared to conventional approaches such as ICP and robust point matching (RPM) [5], CPD demonstrates its superiority in numerous computer vision tasks. However, although the incorporation of a uniform distribution component provides global robustness, localized robustness is desirable in many clinical applications as outliers may be concentrated in a spatial neighborhood. To overcome this limitation [25], proposed a probabilistic point set registration approach based on Student's t-distributions (TMM), which confers the property of localized robustness to the registration process, via estimation of a unique shape parameter for each mixture component in the TMM. Numerous recent studies have employed hybrid shape representations [17–20,23,26], in order to increase the discriminative capacity of probabilistic point set registration approaches. In [26] for example, spatial positions and their associated surface normal vectors were modeled with Student's t-distributions, and Von Mises–Fisher (vmF) distributions, respectively. However, such an approach is ill-suited to registering vessel centerlines, since vmF distributions are not antipodally symmetric. Consequently, they cannot be used to model vessel centerlines as the latter are not consistently oriented in any specific direction throughout the vascular tree.

The applications of interest in this study are vasculature registration for intraoperative brain shift compensation and monitoring the progression of lung disease. Comprehensive reviews on intraoperative brain shift compensation were presented in [1,11]. In general, brain shift can be described as a nonrigid deformation of the brain parenchyma as a result of craniotomy. This phenomenon has a significant impact on the accuracy of neuronavigation systems. Nonrigid registration techniques are employed to warp the preoperative image to its intra- and postoperative counterparts, in order to compensate for brain shit. For example, blood vessel centerlines extracted from preoperative MRIs and intraoperative ultrasound data were aligned by applying the ICP algorithm [27]. In [9,15], CPD was used to compensate for intraoperative brain shift. Both studies used thin plate splines (TPS)-based interpolation to warp the preoperative image to its intraoperative counterparts. Assessing changes to pulmonary vasculature is a crucial for monitoring chronic lung diseases [8,30]. Pathological changes to pulmonary vessels may manifest as pruning of small vessels, dilation of large

vessels, or impaired vessel perfusion. Pulmonary vasculature extracted from longitudinal CT scans are thus compared, to assess treatment response and quantify disease progression [31,32].

As reported in a recent review [16], a major limitation of existing vessel registration approaches is that they are typically designed, and evaluated, for a single application. For example, algorithms incorporating details of the aortic shape [13] cannot be employed for registering cerebral or pulmonary vessels. Furthermore, a generalized vessel registration approach that achieves high accuracy and precision for different applications has not been tackled previously [16], to the best of our knowledge. Consequently, in this study, we propose a novel and generalized framework for registering vessel centerlines. We improve on the HdMM-based vessel registration framework proposed in our recent study [2], through suitable algorithmic modifications, and provide a detailed description of the same. Furthermore, we evaluate the proposed approach comprehensively and compare it with the state-of-the-art, using vascular data from two different clinical applications, namely, intraoperative brain shift compensation, and quantification of pulmonary vascular changes caused by lung disease.

## Methods

An overview of the registration framework is presented in Fig. 1. Vessels are represented as 6-dimensional hybrid point sets comprising spatial positions and their corresponding unit vectors describing local centerline orientation. Here, each voxel representing the vessel centrelines denotes the 3D spatial positions, and the eigenvector corresponding to the smallest eigenvalue of the Hessian matrix [10], is used to represent the 3D local vessel orientation. Hybrid points defining the `Source` are regarded as the centroids of a HdMM, while, the point set defining the `Target` is regarded as data points (observations). The former is registered to the latter by maximizing the log-likelihood (*llh*) function iteratively, using the expectation-maximization (EM) algorithm [6]. The desired affine (translation, rotation and scaling) or nonrigid (displacement) transformations are estimated in the maximization (M)-step. All experiments conducted in this study initially performed an affine registration, and used the estimated transformations to initialize the subsequent nonrigid registration step. In order to cope with large amounts of missing data, we formulated a mechanism for refining the correspondences established between the `Source` and `Target`. This is achieved by clustering and excluding points in the `Source` set that lie within the missing data region in the `Target` set, following both affine and nonrigid registration, henceforth referred to as HdMM+.
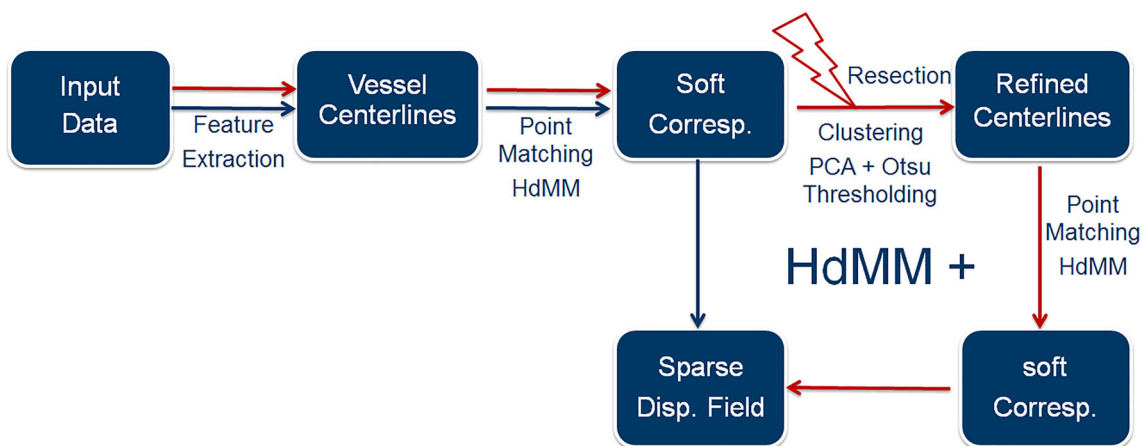
**Fig. 1** Pipeline of proposed framework. The red path shows the steps of HdMM+, while the blue one represents the steps for HdMM

## Hybrid mixture model for vascular structure registration

The proposed hybrid mixture model is a weighted linear combination of two different probabilistic components, where, the Student's t-distribution ($\mathcal{S}$) and Watson distribution ($\mathcal{W}$) are used to model the spatial positions, and vessel centerline orientations, respectively. Following the formulation of TMM in [24,25], the joint likelihood of all $N$ spatial positions in the `Target` centerline points $x_{i=1...N}$ being data points, sampled from an $M$-component TMM (represented by the `Source` centerline points), with model parameters $\Theta_p = \{\boldsymbol{\mu}_j, v_j, \sigma_j\}$, can be described as:

$$p(\mathbf{X} \mid \Theta_p) = \sum_{i=1}^{N} \ln \sum_{j=1}^{M} \pi_j \mathcal{S}(\mathbf{x}_i \mid \boldsymbol{\mu}_j, v_j, \sigma^2) \quad (1)$$

Here, $\boldsymbol{\mu}_{j=1...M}$, $v_{j=1...M}$ and $\sigma^2$ represent the mean positions, degrees of freedom and variance of the Student's t-distributions, while $\pi_{j=1...M}$ represents the mixture coefficient of each TMM component. Considering the antipodal symmetry of the centerline points, we formulate an additional Watson mixture model to model the 3D orientations of vessels. Watson distributions ($\mathcal{W}$) are antipodally symmetric probability distributions defined on a unit-hypersphere, and hence their probability density is the same in either direction along its mean axis. On a $d$-dimensional unit-hypersphere $\mathbb{S}^{d-1} = \{\mathbf{n} \mid \mathbf{n} \in \mathbb{R}^d, \|\mathbf{n}\|_2 = 1\}$, antipodally symmetric vectors ($\pm\mathbf{n} \in \mathbb{R}^d$) are considered to be Watson-distributed, if their probability density function can be expressed as Eq. 2a.

$$p(\pm\mathbf{n}_i \mid \mathbf{m}_j, \kappa_j) = M\left(\frac{1}{2}, \frac{D}{2}, \kappa_j\right)^{-1} \exp^{\kappa_j(\mathbf{m}_j^T \mathbf{n}_i)^2} \quad (2a)$$

$$p(N \mid \Theta_n) = \sum_{i=1}^{N} \ln \sum_{j=1}^{M} \pi_j \, p(\pm\mathbf{n}_i \mid \mathbf{m}_j, \kappa_j) \quad (2b)$$

This distribution is parameterized by the mean orientation $\mathbf{m}$ and the concentration $\kappa$. Here, $M(\frac{1}{2}, \frac{D}{2}, \kappa)^{-1}$ is the confluent hyper-geometric function. This function has been shown to be monotonically increasing within $[-\infty, \infty]$ [29]. With increasing $|\kappa|$, $\mathbf{n}$ are more concentrated along $\mathbf{m}$, for $\kappa > 0$. Consequently, $\kappa$ is often considered to be analogous to the precision of a Gaussian distribution. The joint *llh* of the axes of all $N$ centerline points in the entire `Target` point set, being generated by an $M$-component Watson mixture model (defined by the `Source`) with parameters $\Theta_n = \{\mathbf{m}_j, \kappa_j\}$ is given by Eq. 2b.

We assume both the spatial positions ($\mathbf{x}_i$) and the centerline orientations ($\mathbf{n}_i$) of each hybrid point in the `Target` set to be conditionally independent. Consequently, their joint PDF can be formulated as a product of the individual conditional densities as shown in Eq. 3, where $\Theta_p = \{v_j, \sigma_j\}$, $\Theta_n = \{\mathbf{m}_j, \kappa_j\}$ and $\pi_j$ are the parameters of the HdMM to be estimated. Here, all hybrid points in the `Target` (**T**) are assumed to be independent and identically distributed observations of a HdMM defined by the `Source` point set. The desired transformation parameters $\mathcal{T}$ are estimated by maximizing Eq. 3, in the M-step of the EM-algorithm, in addition to the associated model parameters $\Theta_p, \Theta_n$.

$$
\begin{aligned}
\log(\mathbf{T} \mid \mathcal{T}, \Theta_p, \Theta_n) = &\sum_{i=1}^{N} \ln \sum_{j=1}^{M} \pi_j \mathcal{S}(\mathbf{x}_i \mid \mathcal{T}\boldsymbol{\mu}_j, v_j, \sigma^2) \\
&\times \mathcal{W}(\mathbf{n}_i \mid \mathcal{T}\mathbf{m}_j, \kappa_j)
\end{aligned} \quad (3)
$$

### Affine and nonrigid registration

Pair-wise affine and nonrigid registration is achieved by maximizing the joint likelihood in Eq. 3 using EM. Each hybrid point in the `Target` set is denoted as $\mathbf{d}_i = \{\mathbf{x}_i, \mathbf{n}_i\}$. EM alternates between: the expectation E-step, where the expectations of the posterior probabilities $P_{ij}^t$ are evalu-

ated (refer to Eq. 4a), given an estimate for the model and transformation parameters $\Theta^t = \{\Theta_p^t, \Theta_n^t, \mathcal{T}^t\}$; and the maximization M-step (refer to Eq. 4b), where the estimated $P_{ij}^t$ at the $t$th iterative, are used to update estimates for $\Theta^t$, by maximizing the conditional expectation of the complete data log-likelihood function $Q$, with respect to each parameter.

$$P_{ij}^t = \frac{\pi_j \, p(\mathbf{d}_i \mid \Theta^t)}{\sum_{j=1}^M \pi_j \, p(\mathbf{d}_i \mid \Theta^t)} \tag{4a}$$

$$Q(\Theta^{t+1} \mid \Theta^t) = \sum_{i,j=1}^{N,M} P_{ij}^t [\ln \pi_j + Q(\Theta_p^{t+1} \mid \Theta_p^t)$$
$$+ Q(\Theta_n^{t+1} \mid \Theta_n^t)] \tag{4b}$$

First, we perform an initial affine registration (refer to Eq. 5a) of the vessel centerlines, which is used to initialize the subsequent nonrigid registration step. Here, $P^{\star(t)}$ represents the corrected posterior probabilities estimated in the E-step. Updates for the affine transformation $\mathcal{T} = \{s, \mathbf{R}, \mathbf{t}\}$ and model parameters $\sigma^2$, $\nu_j$ are derived analytically similarly to [25] and computed in the M-step. The model parameters $\kappa_j$ associated with the Watson distributions are estimated using the approximation derived in [4].

$$Q(\Theta_p^{t+1} \mid \Theta_p^t) = \sum_{i,j=1}^{N,M} P_{i,j}^{\star(t)} \left[ -\frac{\|\mathbf{x}_i - s\mathbf{R}\boldsymbol{\mu}_j - \mathbf{t}\|^2}{2\sigma^2} \right.$$
$$\left. + \kappa_j (\mathbf{R}\mathbf{m}_j^T)\mathbf{n}_j \right] \tag{5a}$$

$$Q(\Theta_p^{t+1} \mid \Theta_p^t) = \sum_{i,j=1}^{N,M} -P_{i,j}^{\star(t)} \frac{||\mathbf{x}_i - (\boldsymbol{\mu}_j + v(\boldsymbol{\mu}_j))||^2}{2\sigma^2}$$
$$+ \frac{\lambda}{2} \operatorname{Tr}\{\mathbf{W}^T \mathbf{G} \mathbf{W}\} \tag{5b}$$

Subsequently, the desired nonrigid transformation $(\mathcal{T})$, expressed as a linear combination of radial basis functions (refer to Eq. 5b), is estimated using EM. The associated parameters ($\mathbf{W}$) are computed as described in [22]. Tikhonov regularization is employed to ensure that the estimated deformation field is smooth. In Eq. 5b, $v$ is the displacement field mapping the `Source` to the `Target`, while $\mathbf{W}$ and $\mathbf{G}$ represent the weights associated with the radial basis functions and the Gaussian kernel, respectively. The trade-off between registration accuracy and the smoothness of the estimated deformation field is regulated by $\lambda$.

In CPD and TMM, the Gaussian kernel is computed as $G(\boldsymbol{\mu}_l, \boldsymbol{\mu}_m) = exp^{-\|\frac{\boldsymbol{\mu}_l - \boldsymbol{\mu}_m}{2\beta}\|^2}$. Here, $\beta$ controls the width of the Gaussian kernel and is a hyperparameter that is chosen manually. The value chosen for $\beta$ controls the range of filtered frequencies, and consequently, the spatial smooth-

ness of the deformation field, i.e., higher values result in smoother deformations [22]. However, as it is defined manually, it requires some prior information regarding the degree of smoothness required for accurate registration, or alternatively, tuning of the hyperparameter to identify a suitable value for an application. Furthermore, the same value for $\beta$ is used when computing $\mathbf{G}$, for all points $\mu$, defining the centroids of the mixture model. Consequently, such a kernel has two main limitations - manual definition of kernel width; and enforced global smoothness on the deformation field, as the kernel width is fixed for all $\mu$, when computing $G(\boldsymbol{\mu}_l, \boldsymbol{\mu}_m)$. Our framework addresses these limitations by using the model parameters $\kappa_j$ of the Watson distributions in the HdMM, which represent the concentration of centerline orientations along the mean orientations of each component in the HdMM, to compute a locally adaptive variant of the Gaussian kernel as, $G(\boldsymbol{\mu}_l, \boldsymbol{\mu}_m, \kappa_j) = exp^{-\|2\kappa_j(\boldsymbol{\mu}_l - \boldsymbol{\mu}_m)\|^2}$. The intuition here is that, as $\kappa$ is analogous to the precision (or inverse of the variance) of a Gaussian distribution, it can be used in place of $\beta$ (i.e., the variance of the Gaussian kernel). As all $\kappa_j$ are estimated in the M-step of the algorithm, during the preceding affine registration step, they are automatically defined when computing $G$ for the subsequent nonrigid registration step. Additionally, as $\kappa_j$ is estimated for each component of the HdMM, the resulting kernel is locally adaptive, thereby providing different degrees of smoothness to the deformation field, at different spatial positions.

During nonrigid registration, the transformation parameters $\mathcal{T} = v = \mathbf{G}\mathbf{W}$, and a subset of the model parameters, namely, $\{\sigma_j, \nu_j, \kappa_j\} \in \Theta$ are estimated analytically, via EM. Following EM-convergence, the displacements mapping the `Source` to the `Target` are computed as: $\mathcal{T}(\mathbf{M}) = \mathbf{M} + \mathbf{G}\mathbf{W}$, where, $\mathbf{M}$ represents the means of the HdMM, defined by the former. Since the degrees of freedom $\nu_j$ do not have a closed-form solution, they are estimated iteratively in both registration steps, by the Newton–Raphson scheme, similar to [25].

## Registration refinement

Significant proportions of missing data in the `Source` relative to the `Target`, limits the accuracy and robustness of the propose HdMM-based method. Consequently, we formulated a mechanism for refining the point correspondences, in order to accommodate for the missing data during registration.

First, we construct a 2D feature space for each point in the `Source`. This feature vector is constructed based on the intuition that points lacking correspondence should have low responsibility in describing the `Target` points. This behavior is reflected in the N×M posterior probability matrix estimated following registration using HdMM,

where each entry describes the probability of each point in the `Target` being observations sampled from each point in the `Source` point set. Consequently, `Source` points which are missing in the `Target` point set have a large number of values close to zero in the posterior probability matrix. Furthermore, `Source` points lacking correspondence have large Euclidean distances to the `Target` points, following HdMM-based registration. Therefore, we select the following two features: (1) the number of points in the `Target` set which have posterior probabilities greater than $1e^{-5}$, for each point in the `Source` point set, and (2) the minimum Euclidean distance between each updated `Source` point (use HdMM) and the points in the `Target` point set.

Subsequently, PCA was used to extract the first principal component. Finally, automatic histogram clipping using Otsu-thresholding was performed on the first principal component, to identify and exclude points within the missing data region. The refined correspondences in the `Source` are subsequently nonrigidly registered to the `Target` set using HdMM again (henceforth referred to as HdMM+), to accommodate for the missing data, and improve the overall registration accuracy.

## Experiments and results

### Evaluation metrics

In order to demonstrate the effectiveness of incorporating centerline orientations, and the proposed outlier removal mechanism for registering vasculature, we compare CPD, TMM, TMM+, HdMM and HdMM+, for two different clinical applications. For fair comparison, we fixed the smoothing factor associated with Tikhonov regularization ($\lambda = 1$) during nonrigid registration, for CPD, TMM, TMM+, HdMM and HdMM+ in all experiments. The width of the Gaussian kernel ($\beta$) is set to 1, for CPD, TMM and TMMM+ in all experiments. Following preliminary investigations, we identified 0.5 to be a suitable value for the uniform distribution component weight in CPD, which remained fixed for all experiments. The maximum number of iterations is set to 100 for all methods. Following estimation of the sparse displacement field with the established point correspondence, B-spline interpolation [28] is employed to estimate a dense deformation field and warp the `Source` image.

Modified Hausdorff distance (MHD) [7], and mean surface distance (MSD) [25], are used to quantitatively assess registration accuracy. `MHD1`, `MSD1` compute the MHD and MSD between registered `Source` and `Target` point sets once point correspondences are established; `MHD2`, `MSD2` evaluate the MHD and MSD between the vessel centerlines extracted following warping of the `Source` image to each corresponding `Target` image. Furthermore, 100 homologous

fiducial landmark pairs are defined semi-automatically for each patient, using Murphy's method [21] to assess the mean target registration error (`mTRE`). Since the semi-automatic annotation method in [21] is designed for thoracic CT images, it is not applicable for DSA brain acquisitions. In order to evaluate the degree of overlap in cerebral vasculature following registration of the `Source` images to corresponding `Target` images, for clinical data, we calculate the `Dice` and `Jaccard` coefficients between their respective vessel segmentations.

### Intraoperative brain shift compensation

For intraoperative brain shift compensation, the performance of CPD, TMM, TMM+, HdMM and HdMM+ is compared using both an anthropomorphic head phantom and clinical data. First, vesselness maps of the images are estimated using Frangi's vesselness filter [10]. The vessel centerlines are extracted by applying a homotopic thinning algorithm proposed in [12].

*Phantom data* An anthropomorphic deformable head phantom as described in [3] (refer to Fig. 2) is used to acquire cone beam CT (CBCT) data and conduct synthetic experiments. During the experiments, distilled water is used to fill up the ventricle. We use a 1:10 solution of distilled water and Ultravist 370 as contrast agent to enhance the vascular structures. The embedded tumor is initially inflated with 40 ml distilled water, and downsized to 25 ml, 15 ml, 5 ml and 0 ml subsequently, emulating a tumor resection surgery. In each step, contrast-enhanced cone beam CT image is acquired. All images have a voxel resolution of 0.48 mm$^3$ (refer to Fig. 2 right).

*Clinical data* The clinical data used in this retroperspective study comprises 3D DSA images acquired during tumor resection surgery of a glioma patient. The images are acquired preoperatively, following craniotomy, during resection, and postoperatively, to monitor blood flow within the brain during and after surgery. The surgery is performed in a hybrid operating room with Siemens Artis zeego installation. As with the phantom experiments, the acquisitions have a voxel resolution of 0.48 mm$^3$.

For the phantom data, centerlines extracted from the CBCT images with the tumor maximally inflated (40ml), was treated as `Source` and aligned to the other four remaining acquisitions. In order to validate the performance of the proposed method for brain shift compensation with sufficient amount of clinical data, we include every combination of two, out of four, acquired clinical images as a `Source`-`Target` pair, where the `Source` image is always acquired before `Target` image.

Quantitative results for brain shift compensation are summarized in Table 1. The initial average MSD and MHD are $5.42 \pm 1.07$ mm and $5.57 \pm 1.11$ mm for phantom data, while

**Fig. 2** The computer-aided design model of the anthropomorphic head phantom, the experiment setting and an example slice of CBCT acquisition of the phantom are shown from left to right

**Table 1** Comparison of the accuracy of CPD, TMM, HdMM and HdMM+ for intraoperative brain shift compensation

| | CPD | TMM | TMM+ | HdMM | HdMM+ |
|---|---|---|---|---|---|
| *Phantom* | | | | | |
| MHD1 | $1.04 \pm 0.21$ | $0.61 \pm 0.08$ | $0.41 \pm 0.06$ | $0.56 \pm 0.05$ | **$0.34 \pm 0.03$** |
| MHD2 | $2.16 \pm 0.17$ | $1.85 \pm 0.06$ | $1.77 \pm 0.04$ | $1.81 \pm 0.07$ | **$1.76 \pm 0.05$** |
| MSD1 | $0.97 \pm 0.21$ | $0.58 \pm 0.09$ | $0.32 \pm 0.03$ | $0.54 \pm 0.06$ | **$0.24 \pm 0.02$** |
| MSD2 | $1.83 \pm 0.42$ | $1.20 \pm 0.03$ | $1.15 \pm 0.01$ | $1.19 \pm 0.02$ | **$1.15 \pm 0.01$** |
| *Clinical* | | | | | |
| MHD1 | $2.46 \pm 0.26$ | $1.33 \pm 0.32$ | $1.04 \pm 0.28$ | $1.23 \pm 0.32$ | **$0.90 \pm 0.24$** |
| MHD2 | $4.48 \pm 0.43$ | $1.73 \pm 0.53$ | $1.48 \pm 0.46$ | $1.52 \pm 0.42$ | **$1.37 \pm 0.37$** |
| MSD1 | $2.32 \pm 0.27$ | $1.07 \pm 0.24$ | $0.64 \pm 0.15$ | $0.97 \pm 0.21$ | **$0.55 \pm 0.13$** |
| MSD2 | $3.31 \pm 0.28$ | $1.51 \pm 0.50$ | $1.30 \pm 0.44$ | $1.39 \pm 0.43$ | **$1.26 \pm 0.39$** |
| Dice | $0.28 \pm 0.07$ | $0.72 \pm 0.07$ | $0.74 \pm 0.07$ | $0.72 \pm 0.06$ | **$0.76 \pm 0.05$** |
| Jaccard | $0.16 \pm 0.05$ | $0.56 \pm 0.08$ | $0.58 \pm 0.07$ | $0.57 \pm 0.08$ | **$0.61 \pm 0.07$** |

Mean and standard deviation of all evaluation metrics are summarized in millimeters (mm)
Bold values are used to emphasize the lowest mean and standard deviation

for clinical images, they are $5.40 \pm 1.24$ mm and $5.62 \pm 1.31$ mm. With regard to qualitative assessment of our approach, extracted vessel centerlines from registered `Source` images, are superimposed on its counterpart extracted from `Target` images in Fig. 3. Each row represents the registration result of different `Source` and `Target` pairs, while each column represent a different registration method.

## Pulmonary vascular alternation of lung diseases

For the evaluation of noninvasive disease monitoring of pulmonary diseases, we select baseline (`Source`) and follow-up (`Target`) CT scans of 12 patients from SPREAD study, suffering from pulmonary emphysema [30]. This results in 24 `Source` and `Target` image pairs. All CT images are acquired during breath hold and reconstructed with a standardized protocol optimized for lung densitometry. The slice thickness of the CT images is 2.5 mm and in plane resolution is $0.65 \times 0.65$ mm. The segmentation of pulmonary vessels is performed with a graph cut-based method proposed

in [33]. Subsequent steps including the centerline extraction technique, point matching algorithms, and image warping, are identical to the brain shift compensation experiments.

For all 24 CT image pairs, the initial average MSD and MHD between centerlines extracted from baseline and follow-up images are $8.24 \pm 2.33$ mm and $9.07 \pm 3.7$ mm. Quantitative results after applying CPD, TMM, HdMM and HdMM+ are summarized in Table 2. Examples of overlay between updated `Source` and `Target` point set are presented in Fig. 4.

## Discussion and outlook

The quantitative (refer to Tables 1 and 2) and qualitative (refer to Tables 3 4) results indicate that TMM outperforms CPD significantly, with further improvements achieved using HdMM, compared to TMM. This demonstrates the ability of the proposed registration framework to model fine structural details of both cerebral and pulmonary vasculature. This is attributed to the hybrid representations of vessel centerlines,
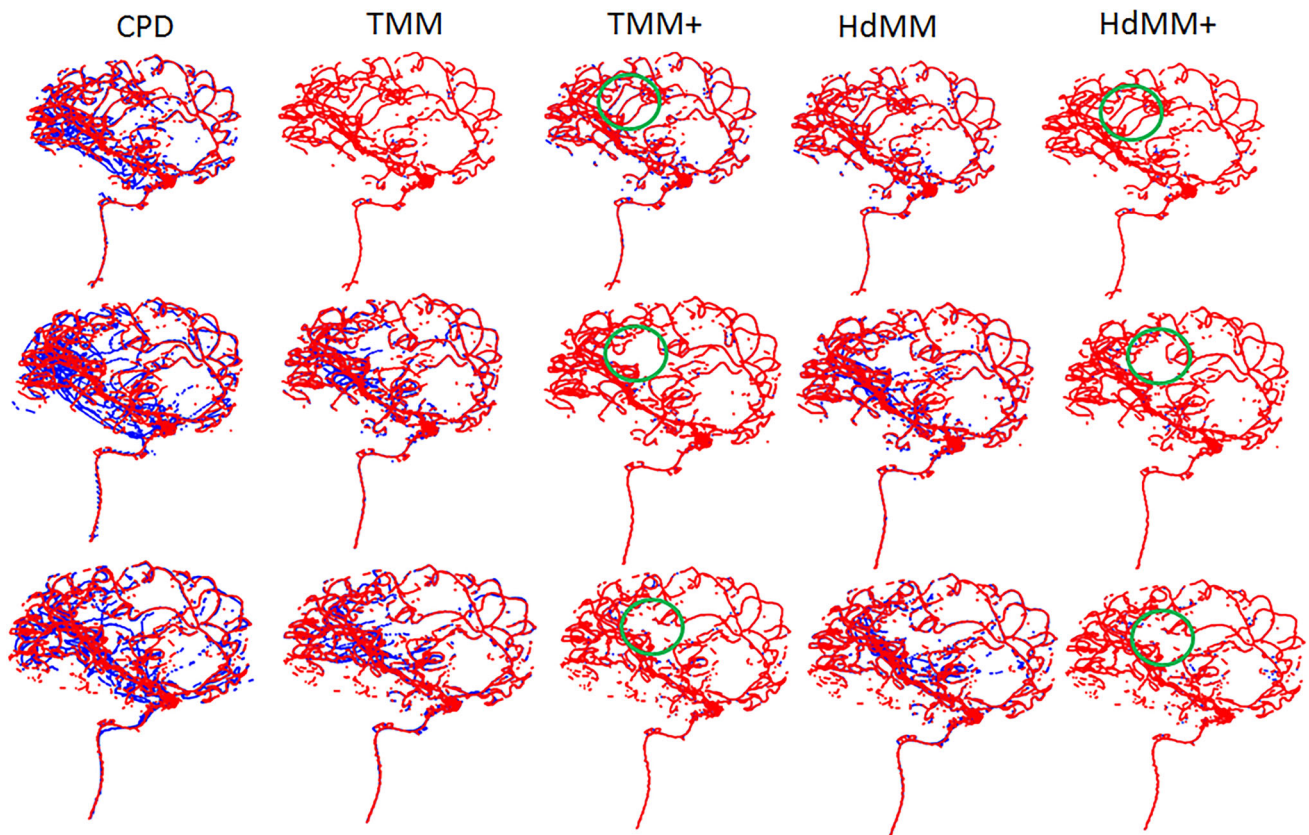
**Fig. 3** Overlay of registered `Source` centerlines (blue) on `Target` (red) point set. The green circle visualizes the location of missing branches caused by tumor resection. The first row shows centerlines extracted from a preoperative DSA image aligned to intraoperative vascular structures following the dura opening. The second row presents the preoperative data aligned with postresectional centerlines. While in the last row, postoperative point set of vasculature is aligned with the intraoperative data following the dura opening

**Table 2** Comparison of the accuracy of CPD, TMM, HdMM and HdMM+ for longitudinal assessment of pulmonary diseases

|      | CPD | TMM | TMM+ | HdMM | HdMM+ |
|------|-----|-----|------|------|-------|
| MHD1 | $3.31 \pm 0.87$ | $2.34 \pm 0.53$ | $1.55 \pm 0.54$ | $2.03 \pm 0.33$ | $\mathbf{1.24 \pm 0.27}$ |
| MHD2 | $4.16 \pm 1.21$ | $2.28 \pm 0.48$ | $2.05 \pm 0.60$ | $2.26 \pm 0.46$ | $\mathbf{2.05 \pm 0.32}$ |
| MSD1 | $3.04 \pm 0.76$ | $2.24 \pm 0.53$ | $1.15 \pm 0.42$ | $1.91 \pm 0.32$ | $\mathbf{0.90 \pm 0.17}$ |
| MSD2 | $3.25 \pm 0.72$ | $2.11 \pm 0.38$ | $1.84 \pm 0.47$ | $2.01 \pm 0.41$ | $\mathbf{1.80 \pm 0.29}$ |
| mTRE | $2.70 \pm 3.45$ | $\mathbf{2.22 \pm 2.85}$ | $\mathbf{2.21 \pm 2.80}$ | $\mathbf{2.20 \pm 2.82}$ | $\mathbf{2.20 \pm 2.82}$ |

Mean and standard deviation of all evaluation metrics are summarized in millimeters (mm)
Bold values are used to emphasize the lowest mean and standard deviation

as they are a rich descriptor of local vessel morphology, and the improved discriminative capacity and locally adaptive nature of the model employed in the HdMM/HdMM+ framework. Complex structures such as vasculature require more descriptive features for accurate registration, than afforded by spatial positions alone. Consequently, a registration framework that jointly models the PDF of spatial positions and centerline orientations, is better equipped for registering complex geometries such as vasculature, than point matching methods that rely on spatial positions alone, regardless of clinical application.

A major challenge in many clinical applications is the presence of missing data due to surgical interventions or pathology-induced morphological changes. The green circle in Fig. 3 highlights the missing branches caused by tumor resection. When registering pre- and postresectional data (refer to row 2 in Fig. 3), missing data poses a great challenge for CPD, TMM and HdMM, whereas TMM+ and HdMM+ are less affected and able to establish correct point correspondences. The correspondence refinement mechanism proposed in our framework identifies a subset of points in the `Source`, which have a large responsibility (i.e., large poste-
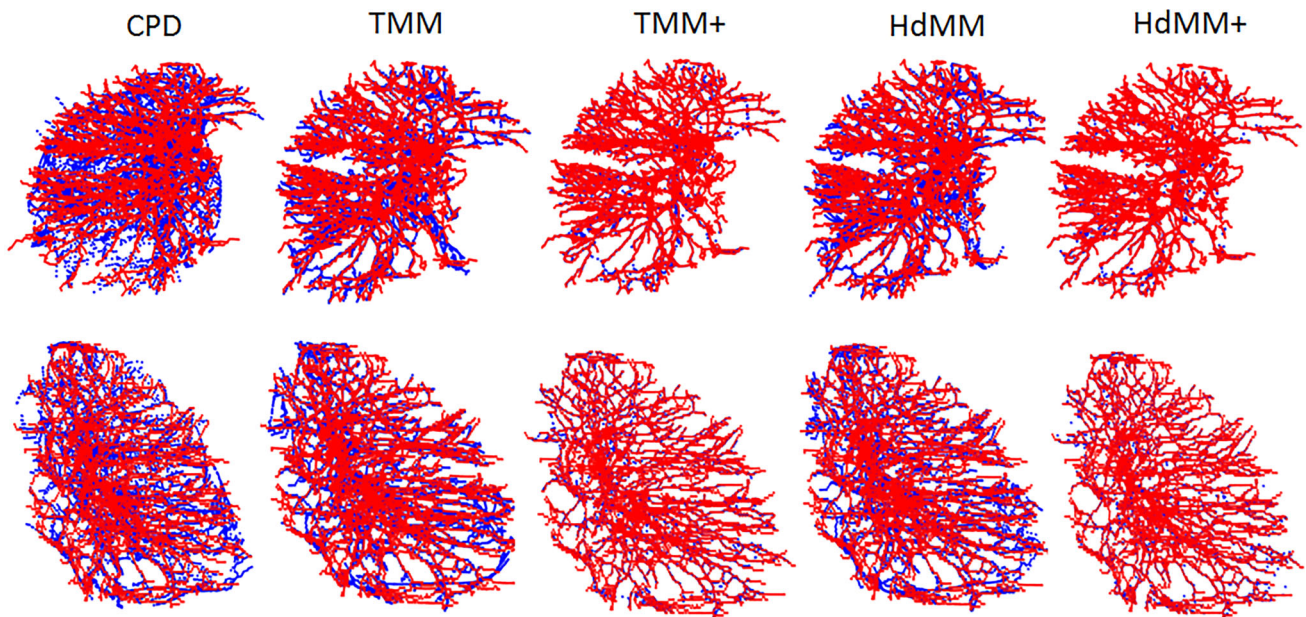
**Fig. 4** Results of the pulmonary vessel registration using CPD, TMM, HdMM and HdMM+. Updated `Source` (blue) point set is superimposed with `Target` (red) data

rior probability) in describing points in the `Target`, without any prior knowledge regarding the positions of missing vessel branches. Following refinement, TMM+ and HdMM+ achieve significant improvements in registration accuracy (refer to Tables 1 and 2) relative to TMM and HdMM, respectively. Overall, HdMM+ consistently outperformed all other methods, in all experiments conducted.

The performance of CPD is affected by three manually chosen hyperparameters (outlier weight, $\beta$ and $\lambda$). While, TMM/TMM+ are affected by just $\beta$ and $\lambda$, as they are inherently robust to outliers due to the heavy tailed property of the constituent Student's t-distributions. However, in the proposed HdMM/HdMM+ framework, $\beta$ is defined automatically using the concentration parameters ($\kappa_j$) estimated for the constituent Watson distributions, i.e., only a single hyperparameter ($\lambda$) remains. Furthermore, as different values for $\kappa$ are estimated for each component of the HdMM, the resulting kernel is locally adaptive, resulting in localized smoothness constraints on the estimated deformation field (as opposed to the global constraint enforced in CPD, TMM and TMM+). The improvements in registration accuracy afforded by HdMM/HdMM+ relative to TMM/TMM+ are attributed to this locally adaptive kernel. Thus, compared to CPD and TMM/TMM+, HdMM/HdMM+ are considered to be of greater practical value within a clinical setting.

Quantitative results presented in Tables 1 and 2 also indicate that `MSD` and `MHD` values are higher, when they are computed following image warping, compared to those evaluated following point set registration. This is attributed to the localized support of B-spline basis functions, used to warp the images. Global deformations introduced by the change

of biomechanical boundary conditions are therefore not considered, when deriving dense displacement fields from its sparse counterparts.

At each bifurcation point, centerline orientation could follow either the main branch or any sub-brunch, i.e., the spatial position and orientation are conditionally independent. This assumption increases the flexibility and the discriminative capacity of the proposed HdMM/HdMM+ framework. However, the proposed framework may be improved by modeling the conditional dependency of spatial positions and associated orientations, for points within each branch. The lack of a "gold standard" for quantitative evaluation of local accuracy is a limitation of the current study. Usually, `mTRE` is the state-of-the-art metric to evaluate the average local accuracy of a registration framework. However, the homologous fiducial landmarks used in this study for the pulmonary data set, is not able to identify differences in the performance of HdMM+ from HdMM and TMM. This is because the homologous landmarks are annotated semi-automatically, where a fixed number of corresponding point pairs are identified without considering missing data. Hence, even if one of the landmarks identified in the `Source` image lacks a corresponding landmark on the `Target` due to pathological changes of the vessels, the semi-automatic approach used, will still identify a point in the `Target`. As the aim of this study was to compare different probabilistic mixture model-based registration approaches, for the task of generalized vessel registration, some aspects regarding the evaluation and algorithmic analysis were beyond it's scope. Future work will look to identify a suitable metric to evaluate the local accuracy of the proposed HdMM+ framework, such

as the performance of missing branch detection for example; conduct a comprehensive analysis of the effect of $\lambda$ on registration accuracy; and qualitatively and quantitatively assess the outlier removal mechanism employed in TMM+ and HdMM+, using manual outlier screening via variogram analysis [14] for example.

## Conclusion

Clinical applications benefit from an accurate and inherently robust registration method, able to accommodate large proportions of outliers, missing data, and morphological variations in vasculature. We treated vessel registration as a point matching problem and formulated a hybrid mixture model-based rigid and nonrigid registration framework. By incorporating a correspondence refinement step to deal with missing data, the proposed HdMM/HdMM+ registration framework was shown to significantly outperform the state-of-the-art, in terms of registration accuracy. We validated our approach using data from intraoperative brain shift compensation, and longitudinal analysis of pulmonary vasculature. The presented results demonstrate the ability of the HdMM/HdMM+ framework to model complex vascular structures acquired from different anatomical regions. The fidelity of the proposed framework is thus compelling for its use in a variety of clinical applications.

## Compliance with ethical standards

**Disclaimer** The methods and information presented in this work are based on research and are not commercially available.

**Conflict of interest** The authors declare that they have no conflict of interest.

**Ethical approval** The study was done retrospectively. It does not contain any studies with animals performed by any of the authors. Brain image data was acquired for clinical purposes. The SPREAD study was approved by local institute broad.

**Informed consent** Informed consent was obtained from all individual participants included in the study.

## References

1. Bayer S, Maier A, Ostermeier M, Fahrig R (2017) Intraoperative imaging modalities and compensation for brain shift in tumor resection surgery. Int J Biomed Imaging 2017:6028645. https://doi.org/10.1155/2017/6028645

2. Bayer S, Ravikumar N, Strumia M, Tong X, Gao Y, Ostermeier M, Fahrig R, Maier AK (2018) Intraoperative brain shift compensation using a hybrid mixture model. MICCAI 2018:116–124

3. Bayer, S., Wydra, A., Zhong, X., Ravikumar, N., Strumia, M., Schaffert, R., Ostermeier, M., Fahrig, R., Maier, A.: An anthropomorphic deformable phantom for brain shift simulation. In: 2018 IEEE NSS/MIC conference record (2018)

4. Bijral, A., Breitenbach, M., Grudic, G.: Mixture of watson distributions: a generative model for hyperspherical embeddings. In: Proceedings of machine learning research (2007)

5. Chui H, Rangarajan A (2003) A new point matching algorithm for non-rigid registration. Comput Vis Image Underst 89(2):114–141

6. Dempster AP, Laird NM, Rubin DB (1977) Maximum likelihood from incomplete data via the em algorithm. J R Stat Soc Ser B Stat Methodol 39(1):1–38

7. Dubuisson M, Jain AK (1994) A modified hausdorff distance for object matching. In: Proceedings of 12th international conference on pattern recognition, vol. 1, pp 566–568

8. Estépar RSJ, Kinney GL, Black-Shinn JL, Bowler RP, Kindlmann GL, Ross JC, Kikinis R, Han MK, Come CE, Diaz AA, Cho MH, Hersh CP, Schroeder JD, Reilly JJ, Lynch DA, Crapo JD, Wells JM, Dransfield MT, Hokanson JE, Washko GR (2013) Computed tomographic measures of pulmonary vascular morphology in smokers and their clinical implications. Am J. Respir Crit Care Med 188(2):231–239

9. Farnia P, Ahmadian A, Khoshnevisan A, Jaberzadeh A, Serej ND, Kazerooni AF (2011) An efficient point based registration of intraoperative ultrasound images with mr images for computation of brain shift; a phantom study. IEEE EMBC 2011:8074–8077

10. Frangi AF, Niessen WJ, Vincken KL, Viergever MA (1998) Multiscale vessel enhancement filtering. MICCAI 1998:130–137

11. Gerard IJ, Kersten-Oertel M, Petrecca K, Sirhan D, Hall JA, Collins DL (2017) Brain shift in neuronavigation of brain tumors: a review. Med Image Anal 35:403–420

12. Lee T, Kashyap R, Chu C (1994) Building skeleton models via 3-d medial surface axis thinning algorithms. CVGIP 56(6):462–478

13. Liao R, Miao S, Zheng Y (2013) Automatic and efficient contrast-based 2-d/3-d fusion for trans-catheter aortic valve implantation (tavi). Comput Med Imaging Gr 37(2):150–161 Special Issue on Mixed Reality Guidance of Therapy - Towards Clinical Implementation

14. Luo J, Frisken SF, Machado I, Zhang M, Pieper S, Golland P, Toews M, Unadkat P, Sedghi A, Zhou H, Mehrtash A, Preiswerk F, Cheng C, Golby AJ, Sugiyama MIII,WMW (2018) Using the variogram for vector outlier screening: application to feature-based image registration. Int J Comput Assist Radiol Surg 13(12):1871–1880

15. Marreiros FMM, Rossitti S, Wang C, Smedby Ö (2013) Non-rigid deformation pipeline for compensation of superficial brain shift. MICCAI 2013:141–148

16. Matl S, Brosig R, Baust M, Navab N, Demirci S (2017) Vascular image registration techniques: a living review. Med Image Anal 35:1–17

17. Min Z, Meng MQ (2018) Joint alignment of multiple generalized point sets with anisotropic positional uncertainty based on expectation maximization. In: 2018 international conference on 3D vision, 3DV 2018, Verona, Italy, pp 170–179

18. Min Z, Wang J, Meng MQ (2018) Robust generalized point cloud registration using hybrid mixture model. ICRA 2018:4812–4818

19. Min Z, Wang J, Meng MQH (2018) Joint registration of multiple generalized point sets. In: Shape in Medical Imaging. Springer International Publishing, Cham, pp 169–177

20. Min Z, Wang J, Song S, Meng MQ (2018) Robust generalized point cloud registration with expectation maximization considering anisotropic positional uncertainties. In: 2018 IEEE/RSJ interna-

tional conference on intelligent robots and systems, IROS 2018, Madrid, Spain, 2018, pp 1290–1297

21. Murphy K, van Ginneken B, Klein S, Staring M, de Hoop BJ, Viergever MA, Pluim JP (2011) Semi-automatic construction of reference standards for evaluation of image registration. Med Image Anal 15(1):71–84

22. Myronenko A, Song X (2010) Point set registration: coherent point drift. IEEE Trans Pattern Anal Mach Intell 32(12):2262–2275

23. Ravikumar N, Gooya A, Beltrachini L, Frangi AF, Taylor ZA (2019) Generalised coherent point drift for group-wise multi-dimensional analysis of diffusion brain mri data. Med Image Anal 53:47–63

24. Ravikumar N, Gooya A, Çimen S, Frangi AF, Taylor ZA (2016) A multi-resolution t-mixture model approach to robust group-wise alignment of shapes. MICCAI 2016:142–149

25. Ravikumar N, Gooya A, Çimen S, Frangi AF, Taylor ZA (2018) Group-wise similarity registration of point sets using student's t-mixture model for statistical shape models. Med Image Anal 44:156–176

26. Ravikumar N, Gooya A, Frangi AF, Taylor ZA (2017) Generalised coherent point drift for group-wise registration of multi-dimensional point sets. MICCAI 2017:309–316

27. Reinertsen I, Lindseth F, Unsgaard G, Collins DL (2007) Clinical validation of vessel-based registration for correction of brain-shift. Med Image Anal 11(6):673–684

28. Rueckert D, Sonoda LI, Hayes C, Hill DLG, Leach MO, Hawkes DJ (1999) Nonrigid registration using free-form deformations: application to breast mr images. IEEE Trans Med Imaging 18(8):712–721

29. Sra S, Karp D (2013) The multivariate watson distribution: maximum-likelihood estimation and other aspects. J Multivar Anal 114:256–269

30. Stolk J, Putter H, Bakker EM, Shaker SB, Parr DG, Piitulainen E, Russi EW, Grebski E, Dirksen A, Stockley RA, Reiber JH, Stoel BC (2007) Progression parameters for emphysema: a clinical investigation. Respir Med 101(9):1924–1930

31. Zhai Z, Ota H, Staring M, Stolk J, Sugimura K, Takase K, Stoel BC (2018) Treatment effect of balloon pulmonary angioplasty in chronic thromboembolic pulmonary hypertension quantified by automatic comparative imaging in computed tomography pulmonary angiography. Invest Radiol 53(5):286–292

32. Zhai Z, Staring M, Ota H, Stoel BC (2018) Pulmonary vessel tree matching for quantifying changes in vascular morphology. MICCAI 2018:517–524

33. Zhai Z, Staring M, Stoel BC (2016) Lung vessel segmentation in CT images using graph cuts. In: Medical imaging 2016